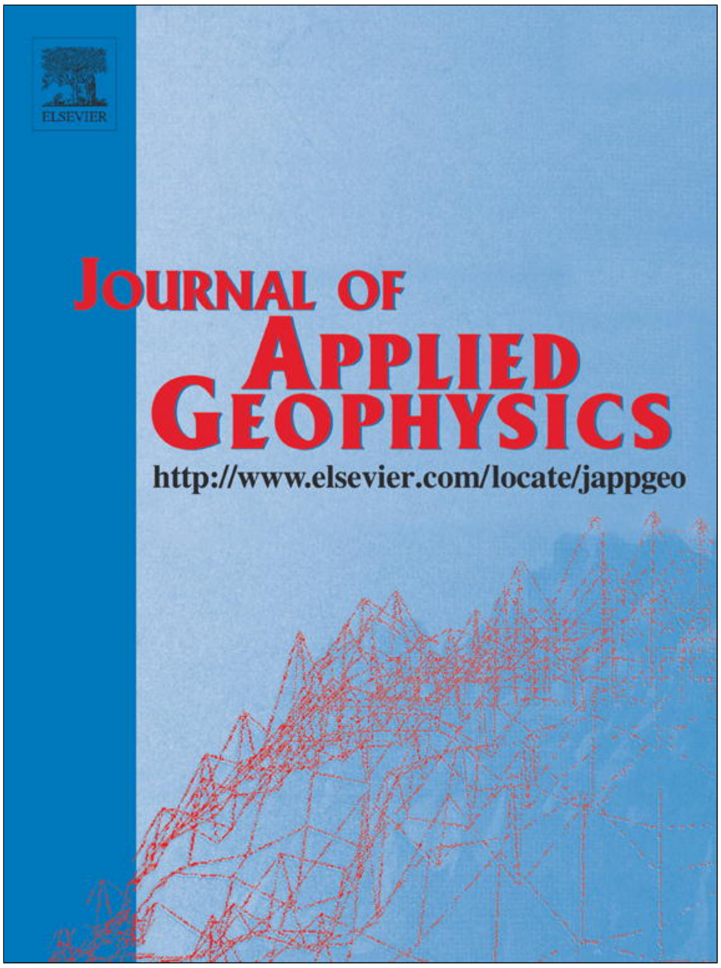
ELSEVIER
JOURNAL OF
APPLIED
GEOPHYSICS
http://www.elsevier.com/locate/jappgeo

Journal of Applied Geophysics 83 (2012) 46–56

Contents lists available at SciVerse ScienceDirect

Journal of Applied Geophysics

journal homepage: www.elsevier.com/locate/jappgeo

Geophysical imaging of shallow subsurface topography and its implication for shallow landslide susceptibility in the Urseren Valley, Switzerland

Stefan Carpentier [a,*], Markus Konz [b,1], Ria Fischer [a], Grigorios Anagnostopoulos [b], Katrin Meusburger [c], Konrad Schoeck [b]

[a] Institute of Geophysics, ETH Zürich, Zürich, Switzerland
[b] Institute of Environmental Engineering, ETH Zürich, Zürich, Switzerland
[c] Institute for Environmental Geosciences, University of Basel, Basel, Switzerland

ARTICLE INFO

Article history:
Received 15 December 2011
Accepted 5 May 2012
Available online 11 May 2012

Keywords:
GPR
Resistivity
GPS
Landslides
Hydrology

ABSTRACT

Landslides and soil erosion are an ever present threat to water management, building construction, vegetation formation and biodiversity in the Swiss Alps. Improved understanding of the mechanics and causative factors of soil erosion is a key factor in mitigation of damage to Alpine natural resources. Recently, much progress has been achieved in the forecasting of landslides on Alpine slopes with a new generation of shallow landslide models. These models perform well in spatial predictions, but temporal control on the occurrence of shallow landslides is less successful. Realistic soil composition and geometry of interfaces are necessary input for better predictions. Geophysical methods have so far not been widely considered to obtain these parameters, in spite of their ability to cover much ground with high-resolution. In this study we successfully use such methods to derive adequate subsurface topography as input to dynamic spatially distributed hydrological and soil mechanical models. Trench, GPS, electrical resistivity tomography and ground penetrating radar data were collected, resulting in revealing images of the composition and geometry of past and future landslides. A conceptual model for the occurrence of local shallow landslides is derived, spanning from block-wise steady creep of detaching soil units to rapid sliding and downslope deposition of soil units via varying sliding planes. Significant topography was observed in the soil interfaces acting as sliding planes, leading to a more complex role of groundwater flow in the initiation of shallow landslides. Hydrogeologic models should be revised accordingly.

1. Introduction

Landslides and rockslides frequently occur throughout most mountain belts worldwide; the Alps in Switzerland are no exception. These slide events vary in intensity from shallow landslides and gradual surface degradation to mass movements in soil and bedrock. The rockslides at the village of Randa in the Matter Valley in 1991 are perhaps the most well-known events in the Swiss Alps in recent times (Green et al., 2006; Heincke et al., 2006; Spillmann et al., 2007; Willenberg et al., 2008). Whereas the devastating effect of rockslides is evident, the effects of shallow landslides are often more subtle, yet far more abundant. Whole slope ranges in populated Swiss valleys are threatened by swarms of landslides. Soil stability plays an important role in ecological, agricultural, hydrological and economic aspects of life.

Realistic forecasting models for shallow landslides are an integral part of their prediction and mitigation. Key static parameters of landslide susceptibility are slope angle, soil composition, soil saturation level and bedrock orientation (Meusburger and Alewell, 2009; Schoeck, 2010). Each of these parameters can be constrained with different methodologies, but until now high-resolution geophysical methods have played a minor role in investigating shallow landslides. In this paper, we advocate the use of such methods by presenting a successful geophysical case study.

First we describe some more conventional methods to obtain static landslide parameters. Slope angle is a property of mountain valleys that can be determined relatively well using GPS, LIDAR, laser-altimetry and other remote sensing techniques, resulting in high-resolution digital elevation models (DEMs). Models with horizontal resolution of up to 2×2 m are suitable for modeling soil creep and shallow landslides (Schoeck, 2010). Soil saturation level can be modeled with advanced algorithms for saturated and unsaturated interflow using river catchment data and realistic precipitation input. Many water flow algorithms exist both in the unsaturated and saturated zone: recent ones have been developed by Fahs et al. (2009) and Anagnostopoulos and Burlando (2011). Realistic simulation of the water flow is crucial since the major triggering mechanism for slope failures is the build-up of soil pore water pressure resulting in a decrease in effective stress and strength

* Corresponding author at: T&A Survey, Dynamostraat 48, 1014 BK, Amsterdam, The Netherlands. Tel.: +31 20 6651368.
E-mail address: carpentier@ta-survey.nl (S. Carpentier).
1 Present address: RMS, Risk Management Solutions, London, UK.

0926-9851/$ – see front matter © 2012 Elsevier B.V. All rights reserved.
doi:10.1016/j.jappgeo.2012.05.001

(Terzaghi, 1943). Furthermore, on steep slopes (as the ones that dominate alpine landscapes) shallow landslides can be triggered by a rapid drop in the apparent cohesion following a decrease in matric suction when a wetting front descends into the soil without generating positive pore pressures (Fredlund et al., 1995; Godt et al., 2009; Lu and Godt, 2008; Rahardjo et al., 1995).

Constraints on detailed soil- and bedrock composition are harder to come by. The weak point in predicting shallow landslides is usually the lack of accurate local geological models required for representative water flow modeling and regionalization of soil strength parameters. Most modelers do not have representative 3-D or even 2-D soil models with spatially varying soil-mechanical and hydrological parameters at their disposal, and they assume parallel-to-slope soil interface topography. In situ and laboratory methods can be used for the determination of soil hydraulic properties and soil shear strength, but these measurements usually represent 1-D samples which provide only limited 3-D support. Geophysical methods do cover large amounts of ground while measuring with high resolution and have the ability to obtain the desired 2-D and 3-D soil interface models. Shallow seismic methods (Büker et al., 1998), ground penetrating radar (GPR; Annan, 2009) and electrical resistivity tomography (ERT; Loke and Barker, 1996) are proven methods that deliver the desired images.

This paper presents results of 2D ERT- and GPR-imaging, trenching, soil sampling and GPS-profiling on the northern slopes of the Urseren Valley near Hospental, Canton Uri, Switzerland (Fig. 1). The target of investigation is twofold: 1) to image and extrapolate the soil- and bedrock composition at past and future shallow landslides above Hospental and 2) to assess how representative current simplified soil-parameterization models for water flow modeling are. After a brief introduction of the site and the regional geology, we discuss the present state of shallow landslide modeling and landslide hazard assessment. The acquisition and processing of the geophysical datasets (GPS, trenches, GPR and

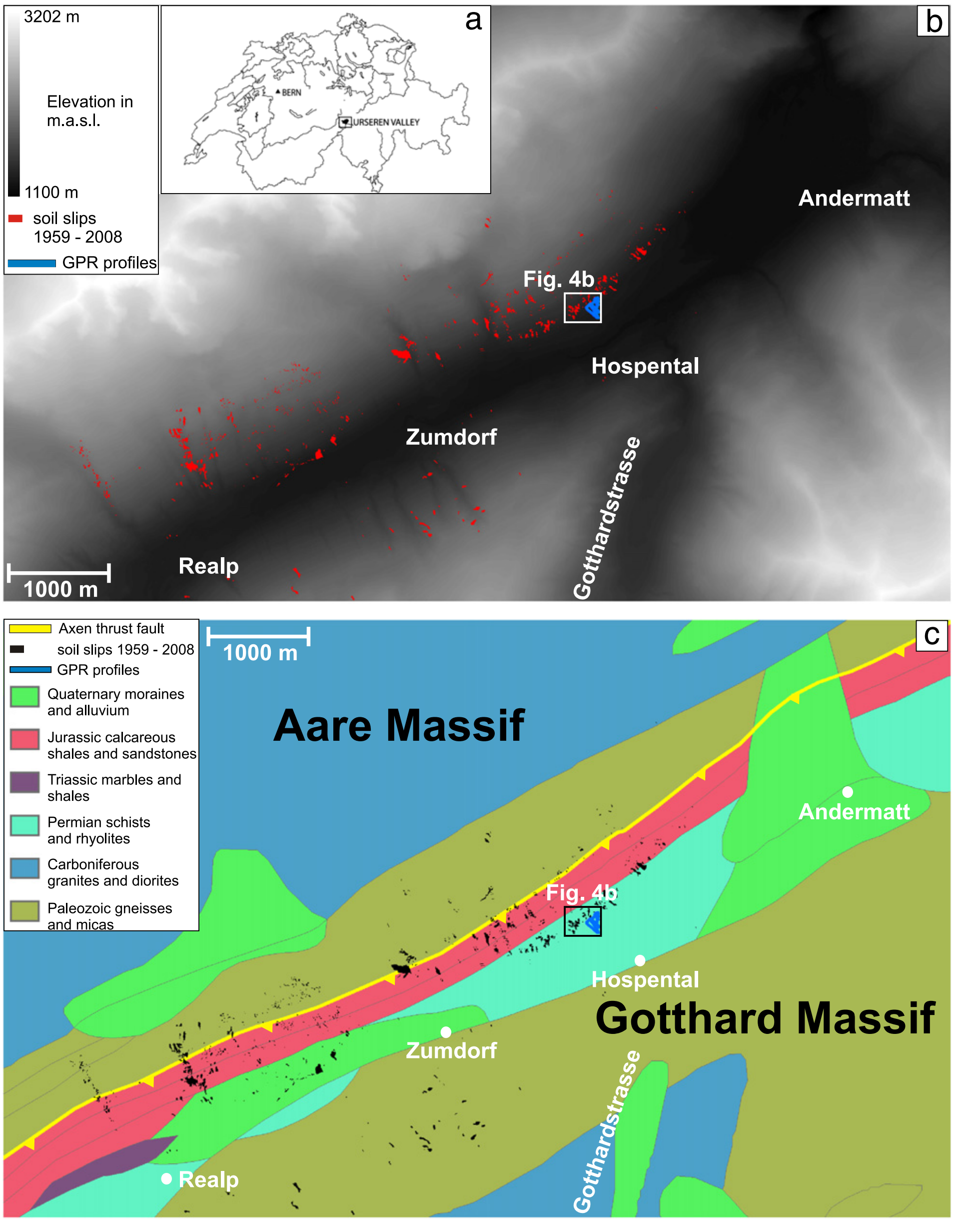

Fig. 1. a) Inset map of Switzerland with location of Urseren Valley indicated. b) Shaded elevation map of Urseren Valley with major towns indicated. The occurrence of shallow landslides in the period 1959–2008 is also shown (red spots), together with the survey site (blue lines in white box). c) Major geological units and source rocks in Urseren Valley (Pfiffner, 2009). The Valley coincides with the Axen thrust Fault, along which the gneisses of the Gotthard Massif are thrust on the granites of the Aare Massif. Shallow landslides (black spots) occur mostly on the steep slopes of the Jurassic and Permian formations. (For interpretation of the references to color in this figure legend, the reader is referred to the web version of this article.)

ERT) are then described, and following this, representative images of all methods are presented in which we interpret mutual subsurface structures. Based on these results, we analyze the local soil composition of shallow landslides and assess the complexity of subsurface topography in soil interfaces along the slopes. Finally, we propose a conceptual model for the occurrence of local shallow landslides and conclude that current simplified hydrogeological models need to take subsurface topography into account.

2. The Urseren Valley

2.1. Regional geology

The Urseren Valley (Fig. 1b) is the earth surface expression of two reinforcing geological processes: a tectonic process and a geomorphological process. In terms of tectonics two crystalline basements of different genesis are juxtaposed on opposite sides of the major Axen thrust fault which runs through the Urseren Valley (Fig. 1c). The Aare System north of the Axen thrust fault, consisting of the granitoid Aare Massif and pre-existing basement, is overthrust by the southerly Gotthard Massif, a younger gneissic intrusive body (Pfiffner, 2009). Between the crystalline massifs a wedge of younger sediments exists, the Urseren Zone, consisting of Permian schists, Triassic marbles, Jurassic calcareous shales and Quaternary alluvium. Since the Urseren Zone is mechanically softer and additionally suffers from fault zone weakening, it is more susceptible to geomorphological processes like glacial and fluvial erosion. The many glaciations (for example the Riss and Würm periods; Cadisch et al., 1948) and downcutting by the current Furkareuss river have shaped the present Urseren Valley. On the slopes of the Urseren Valley, the Urseren Zone is extensively exposed. Shallow landslides on the slopes occur mainly within the bands of Permian schist and Jurassic calcareous shales (Fig. 1b and c; Meusburger and Alewell, 2008). One main causal factor is very likely the soil formation on the weathered products of the schist and shale bedrock: under the influence of water, these bedrocks weather to clay (Blume, 2002). The presence of a clay layer between bedrock and soil, added to significant groundwater flow, is a catalyst for shallow landslides. Geophysical measurements should constrain the extent and geometry of the clay layer for improved landslide modeling.

2.2. Geometry of the Urseren Valley and catchment distribution

Besides the influence of bedrock geology on the formation of shallow landslides, the valley slope angles are another major factor (Fig. 2a). Angles at the bottom of the valley are generally low, but already in the slightly higher part of the valley they quickly increase to 45°. A correlation between slope-angle and the occurrence of shallow landslides is evident, and we further imply a causal relation (Meusburger and Alewell, 2009). An extra factor that contributes to this causality is that water streams, tributary to the Furkareuss river, generally gather in the concentrated gully system on steep slopes. The catchment of the Furkareuss consists of the major source of the river, downstream southwest of Realp (Figs. 1b and 2a) and of the many tributaries northeast of Realp. Especially during snow melt and heavy precipitation, the groundwater flow in the valley slopes and resulting soil saturation are considerable.

3. Assessment of shallow landslide susceptibility with current hydrological models

With information on geology, slope angle and water stream density available, two classes of models for shallow landslide occurrence can be made: statistical and physical models. The majority of statistical models are based on either multivariate correlation between mapped landslides and landscape attributes or general associations of landslides occurrences from rankings based on slope, lithology, landform or geological structure. A recent logistic regression model by Meusburger and Alewell (2009), based on such environmental predictors, performed spatial predictions of shallow landslides resulting in the prediction of 81.4% of the shallow landslides in the Urseren Valley in the year 2000.

The model of Meusburger and Alewell (2009) does not implicitly include predictions on the timing of shallow landslide events. For accurate timing, a physical model is required that can respond to dynamic rainfall and meltwater inputs. A modification on the TOPKAPI model (Todini and Ciarapica, 2001; Todini and Mazzetti, 2008), developed by the Institute of Environmental Engineering of ETH (Konz et al., 2011), provides the modeling framework that is needed for this type of predictions. The TOPKAPI model originated as a fully distributed rainfall flow algorithm. Given a certain DEM, soil information and precipitation input, the algorithm kinematically tracks the transport of water flow between neighboring gridcells. The tracking of the water volume balance is done in space and time from the input water inflow at the highest boundary cells until the outflow at the lowest boundary cells in the grid. An additional shallow landslide routine was implemented in the TOPKAPI model as well (Schoeck, 2010). This routine is based on the infinite slope analysis with the assumption that the slopes are long and continuous, and the thickness of the unstable material is small compared to the dimensions of the slope (Lambe and Whitman, 1979). Per gridcell, this routine evaluates the shear stress of the soil and compares it to the shear strength. If the shear stress exceeds the shear strength, that gridcell reports failed soil stability implying a shallow landslide. The shear conditions are a function of among others: slope-angle, soil composition, soil depth and groundwater pressure head. To make estimates about the probability of failed soil stability and therefore shallow landslides, a measure for the susceptibility of soil in a cell to fail was established. It is defined per gridcell as the number of total soil failures that occur in time, divided over the total amount of time(-steps). This ratio varies between zero and one, and in case of the latter, an extremely susceptible and thus permanently unstable soil is present. Such a shallow landslide susceptibility map was computed for the Urseren Valley according to the algorithm of Schoeck (2010), and it is displayed in Fig. 2b. This map has captured 85.6% of all observed shallow landslides in the year 2000: a marginal improvement with respect to the model of Meusburger and Alewell (2009) which correctly predicts 81.4% of the shallow landslides.

Several assumptions are made for the implementation of the shallow landslide extension to TOPKAPI. It is assumed that a type of soil has an associated set of constant soil properties (porosity, density) per gridcell. Another assumption is that the soil-bedrock interface is always parallel to the surface, being essentially 1D, and that soil depth is constant per gridcell. Especially the latter assumption is a strong one and is probably the reason that the timing of the shallow landslides is inaccurate in the current shallow landslide algorithm. The geophysical images resulting from our geophysical survey can confirm or disprove the assumption of 1D constant parallel-to-surface topography of the soil layer.

4. Geophysical measurements

4.1. Data acquisition

During geophysical surveys on the valley slopes above Hospental in the summers of 2006, 2009 and 2010, independent measurements of ERT-, GPS-, GPR- and trench data were done. On Figs. 1 and 2 the survey location in the Urseren Valley is indicated. One ERT profile, 36 GPR profiles, 6 trenches and associated GPS coordinates spanned a survey area of about 250 m times 200 m. Several past shallow landslides are visibly present in this area and the majority of profiles crossed a number of suspected soon-to-fail shallow landslides as well. Fig. 3 shows an example of a GPR measurement in progress at the top of a past shallow landslide on a $\pm 40°$ slope. The GPR antennas were mounted on a plastic sled in a parallel broadside configuration.

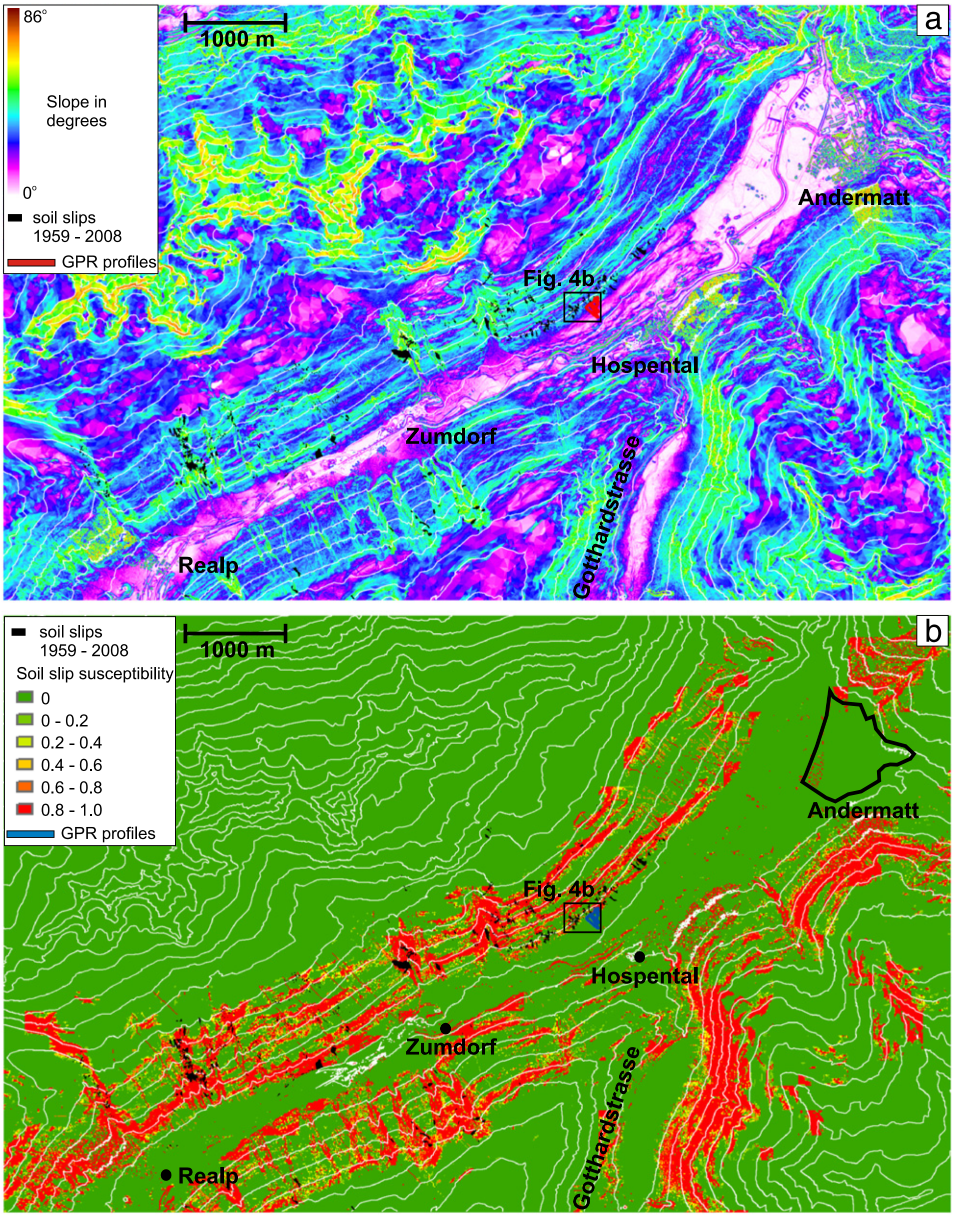

Fig. 2. a) Slope-angle map of Urseren Valley. Note that shallow landslides (black spots) occur exclusively on steep (>40°) slopes, but not all steep slopes cause shallow landslides. The underlying hydrology is of paramount influence on shallow landslide activity. b) Shallow landslide susceptibility map as derived by Schoeck (2010). Observed shallow landslides are spatially well predicted by the susceptibility model, which combines slope information with river catchment analysis and detailed hydrological modeling. Temporal prediction is so far less successful.

ERT and GPR profiles of 20–140 m could be collected throughout the survey area, except at places with dense bush coverage (see Figs. 3 and 4). The ERT data were collected with a Syscal Kid system, and GPR data were collected with a PulseEKKO Pro system and the GPS data used Novatel equipment. Trenches were dug on a past landslide, next to a series of closely spaced parallel GPR profiles upslope. Detailed acquisition parameters for the ERT and GPR data are listed in Table 1.

Because of the challenging terrain and the high-resolution nature of the data, precise and absolute coordinates are required for every measurement to perform proper data processing and to achieve a combined interpretation. The absolute locations and labels of all the profiles are displayed in Fig. 4: a photo of the slopes, past shallow landslides and vegetation gives context to the profiles in Fig. 4a, whereas elevation contours, precise locations and labels are drawn in Fig. 4b.

4.2. Data processing

The multitude of geophysical methods required custom data processing steps. GPS data were post-processed by combining differential solutions of a remote measuring unit and a base station. This delivered absolute coordinates with ±3 cm precision (Fig. 4).

ERT data from profile e1 (Fig. 4b) underwent initial quality control (removing noisy and poorly coupled electrode-measurements) after which the data and geometry were input to a tomographic inversion algorithm, part of the RES2Dinv software package (Loke and Barker, 1996). After sufficient inversion iterations, the root-mean-square (RMS) data misfit dropped to a minimum of 5.7%.

The GPR reflection data were acquired at two dominant frequencies, 100 MHz (profiles a1–a20, Fig. 4b) and 250 MHz (profiles b1–b16, Fig. 4b). The GPR data were subjected to processing algorithms very similar to those in seismic reflection imaging. A Dewow (high-pass,

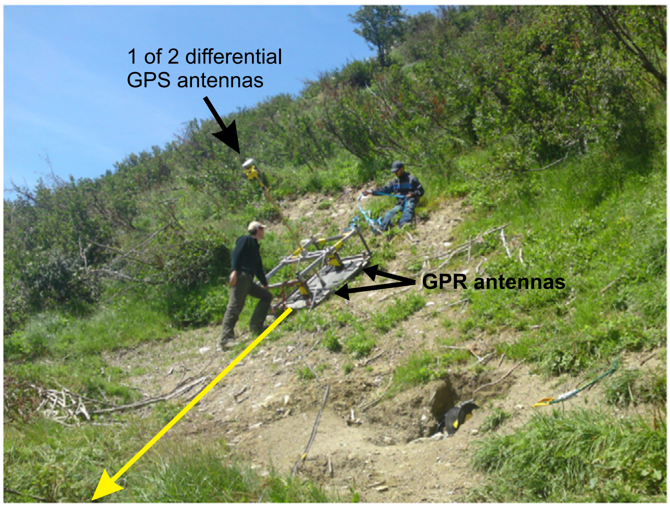

Fig. 3. Photo of ground penetrating radar acquisition setup. The steep slopes posed a significant acquisition challenge, here for a 100 MHz GPR profile. With the help of ~3 cm precise differential GPS positioning, ultra high resolution GPR profiles could be produced.

median) filter was applied to the recorded GPR traces to compensate for the signal saturation on the antennas, after which a time-zero correction put the onset of the signals at the theoretical start time. The signal attenuation by geometrical spreading and by conductive ground was compensated by amplitude scaling, in this case an automatic gain control (AGC) with 20 and 10 ns windows for the 100 and 250 MHz data respectively. An Ormsby bandpass filter with corner frequencies of 30–50–110–130 MHz (100–120–300–350 for the 250 MHz data) removed noise outside of the source frequency spectrum, and a spatial median filter along the traces removed reverberation artifacts. Through the process of trace equalization subtle trace-by-trace variations in recording gain, caused by varying antenna coupling along the profile, could be corrected. This enhanced coherency was of benefit to the performance of the subsequent phase shift migration (Gazdag, 1978), which repositioned reflected energy in the GPR section to its true reflection point. The last step in the processing scheme was time-to-depth-conversion of the migrated section in time. Using an average radar-wave velocity of 0.1 m/ns, representative for loamy sand at our survey site, the final GPR depth-images were generated.

Lastly, six trenches (T1–T6, Fig. 4b) were dug next to two representative GPR profiles, a9 and a8. These trenches had a width and depth of about 1 m and 2.5 m respectively, and they were photographed and categorized into soil layers and associated soil composition.

5. Results and interpretation

5.1. Trench sections

From the six trenches, detailed observations concerning depth, interfaces and other parameters of the soil were gathered and used as constraints for further interpretations. Examples of trench results, in the form of photos, can be seen in Fig. 5. There, the complete soil column up to the top of the bedrock is sampled. Five main units could be consistently classified in the trenches, from top to bottom: 1) a $\pm$0.7 m loamy sand layer, 2) a $\pm$0.05 m xenolithic schist layer, 3) 1.5 m of clayey sand, 4) a $\pm$0.1 m pure clay layer and 5) fractured bedrock. Yellow annotation denotes the five units in Fig. 5, and black arrows mark the continuous clay layer in the neighboring trenches (insets). The xenolithic schist layer, clay layer and fractured bedrock are all major soil interfaces and are known to act as hydrological boundaries. Depths to these interfaces were seen to vary in the order of 0.5 m from trench to trench, already indicating significant subsurface topography. These subsurface undulations are independent of the strong surface topography, including bumps and cracks close to the trenches. At the time of excavation of the trenches, no water or high levels of moisture were observed in any of the trenches, but conditions were dry at the time. No signs of organic material were present as well, probably due to the nature of the eroded source rock and because of the active recycling of soil on the slopes. Together, these observations point to a highly dynamic layer of soil on top of the bedrock. Soil appears to be in steady motion, leading to compressed and dilatated zones in the soil layer expressed as bumps and cracks at the surface. The soil appears devoid of organic material, allowing relatively fast drainage of water trough the sandy layers in case of flooding by rain or melt water. The subsurface topography in especially the clay layer is expected to have a large impact on this drainage as it acts as impermeable layer which defines the maximum penetration depth of percolating water. Thus, it is critical for over-pressure distributions in the soil layer above.

5.2. GPR profiles

5.2.1. GPR profiles at top of slope

Soil interface observations in our trenches can be at best considered as 1-D depth-sections. Both the GPR and ERT measurements will image contrasts in electric properties of the soil over the whole spatial extent of the suspected shallow landslides. The schist layer, clay layer and fractured bedrock as observed in the trenches should show up as major dielectric contrasts. Fig. 6 confirms this with 250 MHz GPR section b3 (Fig. 4b), which underwent the data processing sequence as described in Section 4. Several strong and continuous GPR reflections can be traced through the section (Fig. 6a) at depths below the surface of ~1 m, ~2 m and ~2.5 m. The shallowest continuous reflection (~1 m) is also the weakest of the three. A very strong and continuous reflection appears at ~2 m depth and below that, a relatively strong but less continuous reflection occurs (~2.5 m). We presume that the upper reflection represents the xenolithic schist layer (green line, Fig. 6b), being a thin and low-contrasting layer. The pure clay layer is thick and well-defined in all trenches, making for a large and consistent contrast as the second reflection indicates (yellow line). Fractured bedrock, as seen in the trenches, is a large dielectric contrast as well but the rough surface of this interface will cause a less continuous reflection, as the one at $\pm$2.5 m depth (black line). In Fig. 6b their significant topography, independent of the surface topography, becomes evident. A general trend of shallowing interfaces downslope is present, resulting in decreased GPR depth penetration due to the shallowing pure clay layer.

Another prominent feature is the interruption of the direct wave, the very first arrival in the GPR section. This wave, traveling along the soil surface directly between source and receiver, is discontinuous at $X=15$ m. An outtake from the GPR section at this location, with its elevation correction removed (black box in Fig. 6a), shows the break in the direct wave more clearly (within black ellipse). During acquisition along the b3 profile a hint of a surface crack was already present at this location. Such a surface crack constitutes an air-filled cavity which acts as a total reflector for the direct wave. The break in the direct wave was consistently crossed by all profiles b1–b7 (Fig. 4b) suggesting that the crack is the upper boundary of a potentially unstable patch of soil.

Below bedrock depth, high variability in reflection strength is visible. Truncations in reflectivity between $X=1$–$X=4$ m and $X=10$–$X=11$ m (Fig. 6b) indicate strong heterogeneity in the bedrock, which is not a usual phenomenon. The unmigrated GPR sections, both 100- and 250 MHz (not shown here), feature an abundance of diffraction hyperbolas at these locations. Given the fact that the structural dip of the local Permian schistose bedrock is near-vertical (Wyss, 1986), we are most likely looking at interbedding within the bedrock.

GPR section b5 (Fig. 7b) further to the northeast (Fig. 4b) features the same interpreted horizons and interrupted direct wave as section b3. All three soil interfaces run deeper in profile b5 than in b3, but have an identical shallowing trend downslope, including the reduced

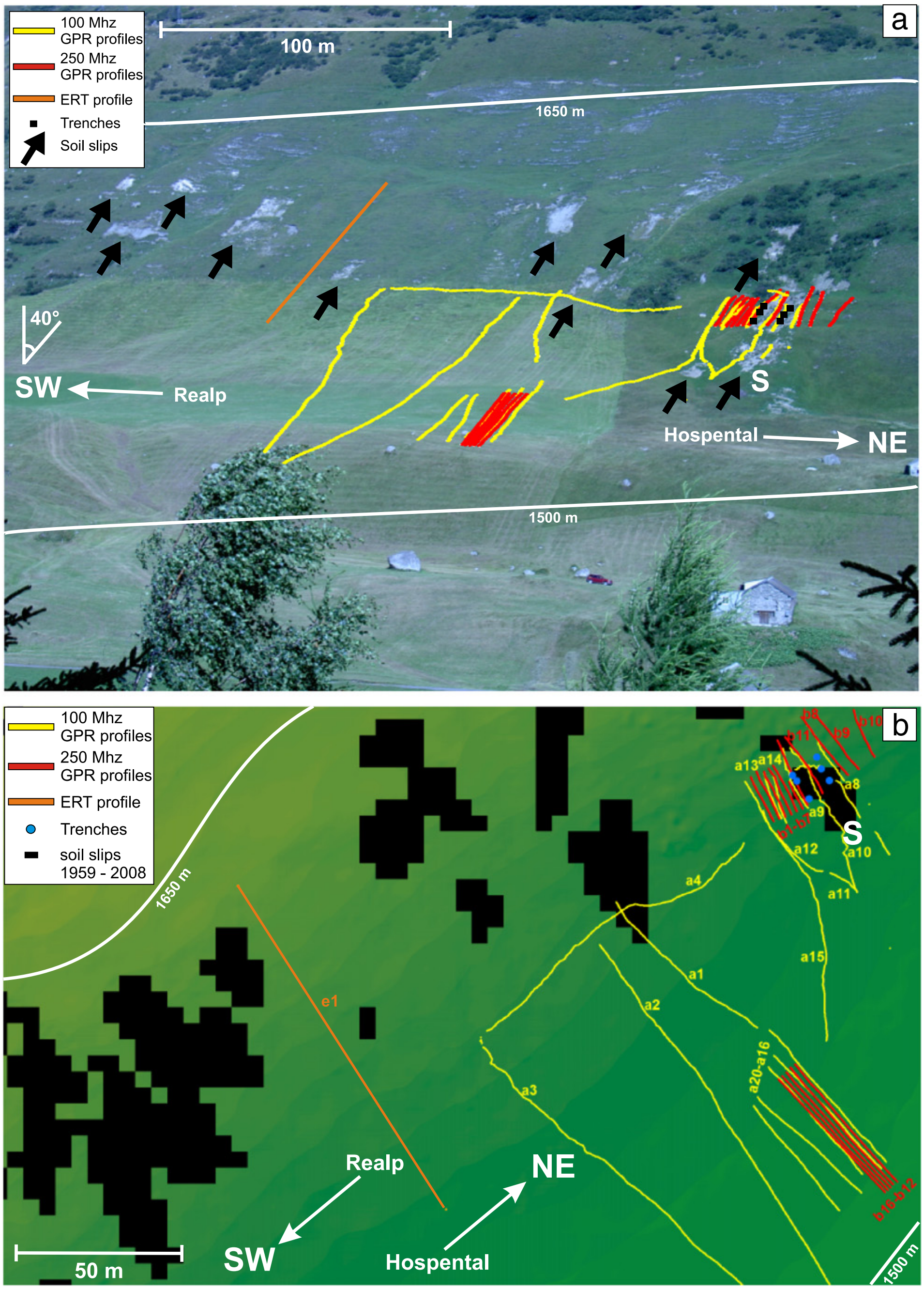

Fig. 4. a) Photo of survey site, taken from the opposite (SE) side of the Urseren Valley. Profiles were acquired at representative positions in the survey area, with focus on the past shallow landslide 'S' at the center right and on the base of the slopes at the center bottom. White contour lines denote elevation. b) Detailed plan view of GPR profiles, ERT profile and trenching locations. Labels denote the profiles as they are mentioned in the later figures and text. Note the dense GPR sampling of the past shallow landslide 'S' by lines b1–b11 and a8–a14. White contour lines denote elevation. (For interpretation of the references to color in this figure legend, the reader is referred to the web version of this article.)

GPR depth penetration. Indications for truncated reflectivity below the bedrock are weaker, but are enough to interpret as vertical internal beds.

5.2.2. GPR profiles at base of slope

An additional set of GPR profiles were collected at the base of the shallow landslide area, where the slopes are much less steep. The subsurface reflectivity is very different at this location, as demonstrated by 250 MHz GPR section b16 (Fig. 4b) in Fig. 8. Reflection strength, continuity and depth penetration have markedly increased, allowing for the imaging of strongly curved horizons close to the surface at the far base of the slopes. We observe subhorizontal, banded reflectivity which points to either well-developed strata in the bedrock or to stacked colluvial/shallow landslide units. Due to the dominant vertical dip of the local Permian schistose bedrock (Wyss, 1986) we rule out bedrock strata, which leaves soil deposits as the most likely candidate. Whether these soil deposits are past shallow landslides or long-term colluvial deposits cannot be determined from these data alone. Their curvature and an offset truncation at $X = 17$ m suggest strong compressional deformation of the layers, which we have interpreted with an overthrust fault (Fig. 8b). This process can be part of overall valley bulging at the base of the valley.

5.3. ERT profile and overlapping GPR profile

Our study area is bounded upslope to the west by ERT profile e1 (Fig. 4b). We will discuss the area between e1 and GPR profile a2 through a combined interpretation of these two profiles. When comparing these

Table 1
Data acquisition parameters.

2D ERT data	
Number of lines	1
Number of electrodes	28
Electrode spacing	5 m
Inverted line length	140 m
2D GPR data	
Nominal frequency	100/250 MHz
Antenna configuration	(Un)shielded, broadside parallel
Antenna separation	1.0/0.4 m
Time window	800/400 ns
Sample rate	0.8/0.4 ns
Number of lines	16/20
Trace spacing	0.2/0.05 m
Line lengths	20 to 140 m

two types of measured quantities (ERT: resistivity and GPR: dielectric constant), we should focus on a soil type that is highly contrasting in both quantities. Clay-rich soil is a prime candidate for that, as it sets itself apart with very low resistivity (1–100 Ω m) and a very high dielectric constant (7–43) (Telford et al., 1990). The solid schistose bedrock below the clay-rich soil is expected to have a resistivity well above 120 Ω m (Telford et al., 1990), providing for a distinguishable contrast. When inspecting the resistivities in the ERT profile e1 in Fig. 9, a delineation can be made on basis of a resistivity-isoline, in this case 135 Ω m (black line). This value should set the solid schistose bedrock apart

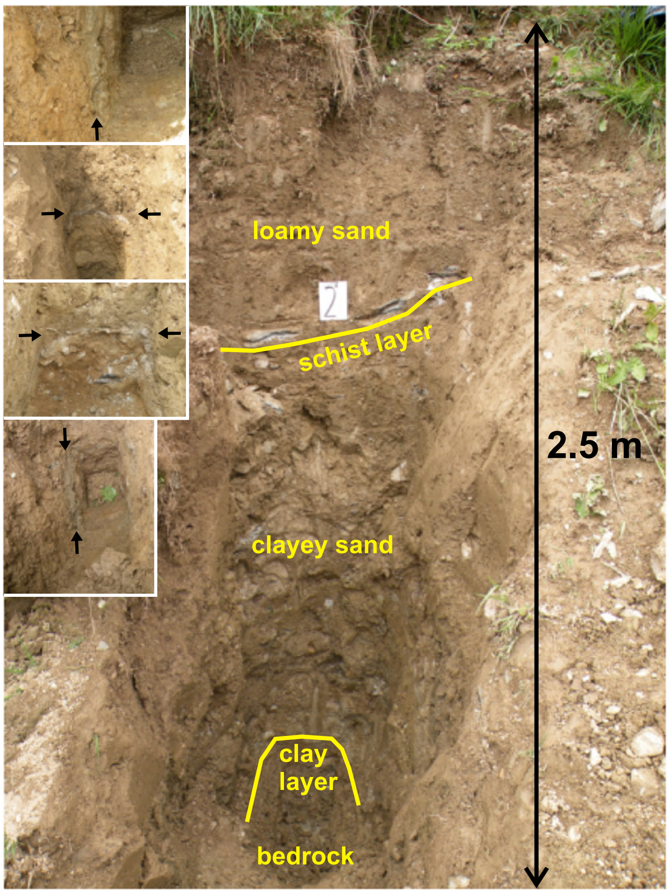

Fig. 5. Photo of trench T2. Notable soil interfaces can be identified as well as soil facies between the interfaces. Depths and dips of especially the xenolithic schist-layer, erosional clay layer and weathered bedrock pin down the interpretation of the GPR profiles. The small photo insets emphasize the nature of the clay layer in neighboring trenches (black arrows).

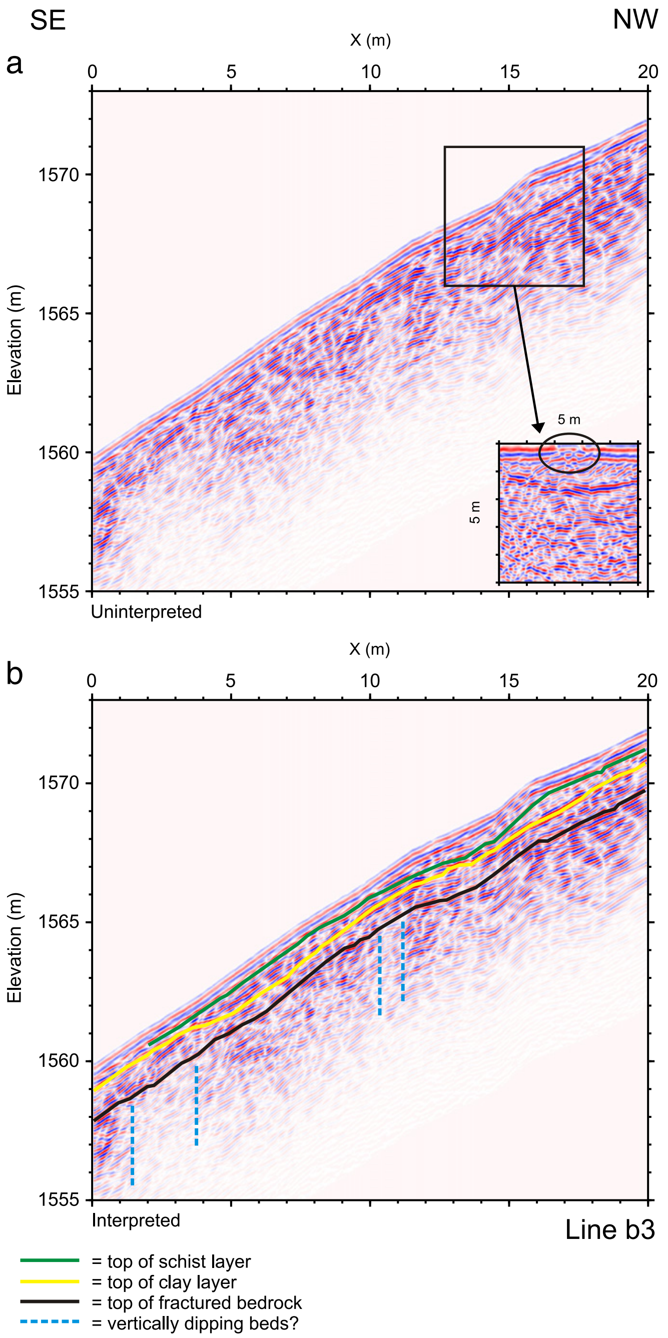

Fig. 6. a) Uninterpreted 250 MHz GPR profile b3. Profile b3 is located just SW of the past shallow landslide 'S' (Fig. 4), on a patch of soil which is likely to fail soon. A surface crack hinting to this future landslide can be seen in a version of the GPR data without elevation–correction (black box and arrow). Note the interrupted ground wave in the ellipse. b) Interpreted profile b3. The schist layer (green) and clay layer (yellow) are seen as strong and semi-continuous reflections. Likely weathered bedrock (black) is marked by deeper bands of less continuous reflections. Note the significant topography in both schist and clay layer, which is independent of the surface topography. (For interpretation of the references to color in this figure legend, the reader is referred to the web version of this article.)

from the clay-rich soil. Indeed a shallow layer of 1–5 m with very low resistivities (30–90 Ω m, blue-ish colors) is seen to overlie a massive deeper block of high resistivity (250–1000 Ω m, yellow-brown colors). The 135 Ω m isoline is assumed to represent the top of the solid bedrock.

Strong topography characterizes the isoline, indicative of undulating interfaces within the overlying soil unit (marked by thin black arrows). Between $X=160$ and $X=170$ m, a patch of high resistivities interrupts

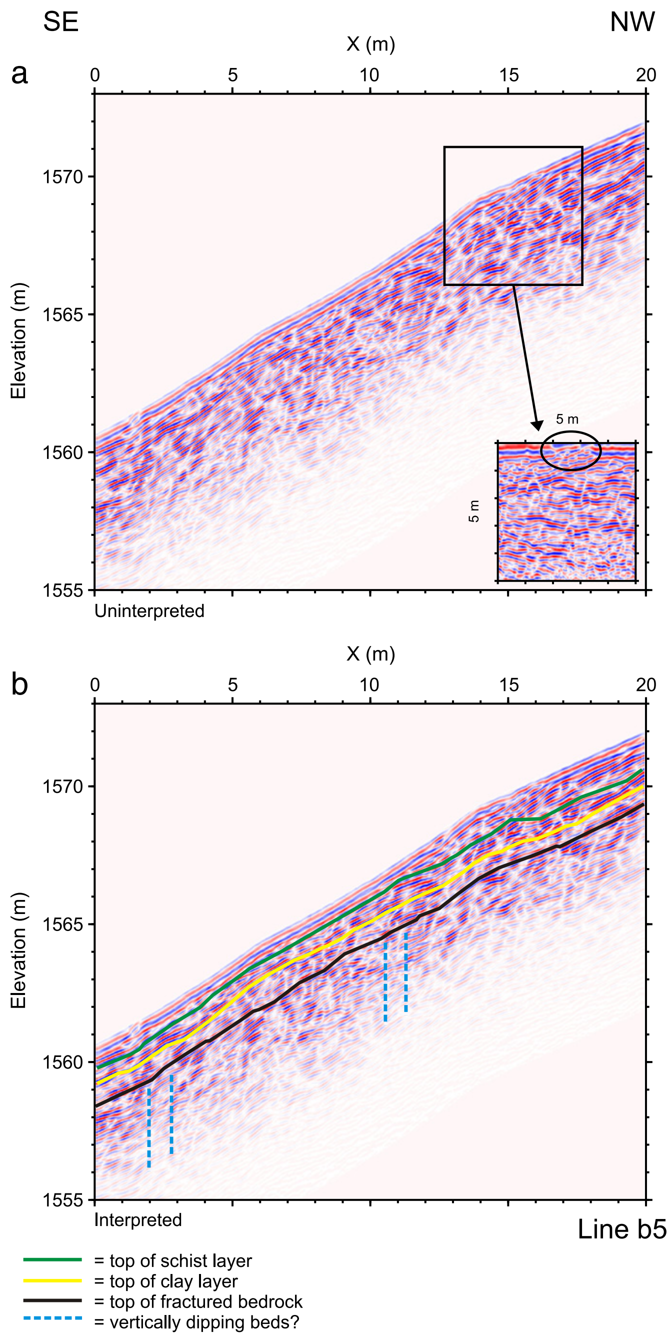

Fig. 7. The same as in Fig. 6, but now for 250 MHz GPR profile b5 (Fig. 4).

the low resistivity upper layer. The most likely explanation for this is either the presence of multiple surface cracks or surfacing bedrock. Within the deeper block of high resistivities, some lateral heterogeneity appears to be present too, which could be due to the vertical interbedding in the schistose bedrock. The resolution of the ERT profile at this depth is insufficient however to be conclusive about this possibility.

100 MHz GPR profile a2 was acquired down the same slope, overlapping with the ERT profile e1. It principally shows the same features (Fig. 9) as identified in the 250 MHz GPR profiles b5 and b16 (Figs. 7 and 8): shallow and short-wavelength undulating reflections on the higher part of the slope and thick bands of long-wavelength folded reflectivity at the base of the slope. From top to bottom of the total slope, a clear increase in signal depth-penetration is visible (marked by black line), suggesting that the clay-rich content of the soil runs deeper at the base of the slope. In the overlap on the highest part of the slope the black line marking the end of GPR penetration corresponds remarkably well in depth with the top of the solid bedrock as inferred from the ERT section. It is not far-fetched to assume that they represent the same interface, which implies independent confirmation by two methods that significant topography in the subsurface clay layer is present.

6. Discussion

6.1. Conceptual model for local shallow landslides

As one of the objectives in this study, we pursue a combined interpretation of all geophysical data in terms of soil composition and a conceptual model for the occurrence of local shallow landslides on the lower slopes in the Urseren Valley. A summarizing sketch in Fig. 10 combines the major observations from the GPS, ERT, GPR and trench data.

The model has a basis of interbedded bedrock (Fig. 10, gray unit). Based on literature (Wyss, 1986) and the lateral discontinuities at bedrock depth in the GPR and ERT sections, we infer a sub-vertical interbedded sequence marked by the dashed black lines. This interbedding has large implications for the overlying soil layer: since the different vertical beds most likely have different mechanical strengths and thus weathering properties, the depth and thickness of the overlying soil cover can strongly vary laterally. This is in good agreement with the lateral subsurface topography of the clay-layer at the base of the soil unit as observed in the trenches, GPR and ERT images. The slipping movement of the soil-layer can be influenced by the vertical beds as well. If we assume that in between large sliding events, steady creep slowly moves the soil cover downslope, the lateral differences in weathered bedrock will have an impact on this creep. Certain parts of the soil-layer along-slope will move faster whereas other parts may be nearly locked (large black arrows), causing differential stress build-up internally in the soil layer. This could explain the undulating clay-layer: folding by compression. The cracks in the soil-layer, observed at the surface and in the GPR data, support the idea of creeping and locked patches of soil on the slopes. Where soil-patches creep (large black arrows), they detach from patches that are locked, causing the observed cracks.

When sufficient groundwater-flow is present, for example during or after massive rain-fall or meltwater events, the shear-strength of a soil interface such as the clay-layer will drop sufficiently to trigger a shallow landslide. The pure clay-layer is not the only candidate however for a shallow landslide sliding plane. From the trenches a continuous xenolithic schist layer was observed, probably emplaced in the soil-layer by a large historical rock-slide. The schist layer is continuous to such an extent that it can guide groundwater flow and function as a sliding plane for shallow landslides. The most recent shallow landslide at our survey site in October 2008, tagged 'S' in Fig. 4, has in fact slid along this schist layer.

When a shallow landslide does occur and its mechanical momentum is large enough to carry far, it gets dumped at the base of the steep slopes (Fig. 10, 'shallow landslide deposition zone'). This is a good explanation for the thick sequence of low-attenuative layers that we see in GPR profiles a2, a3, a16–a20 and b12–b16 at the base of the slopes (Figs. 4b, 8 and 9). The curved horizons are then caused by compression due to shallow landslide load and gravity pull on the soil layer along-slope. This can be considered a process similar to valley bulging. Given the low attenuation in these layers, the pure clay-layer and underlying bedrock are inferred to run very deep here.

6.2. Topography of clay layer and implications for groundwater flow

Large topography in the clay-layer on top of the fractured bedrock was observed in trenching-, GPR- and ERT sections. This topography occurs independent of the slope surface and likely has more to do with bedrock interbedding and soil-compression than with surface

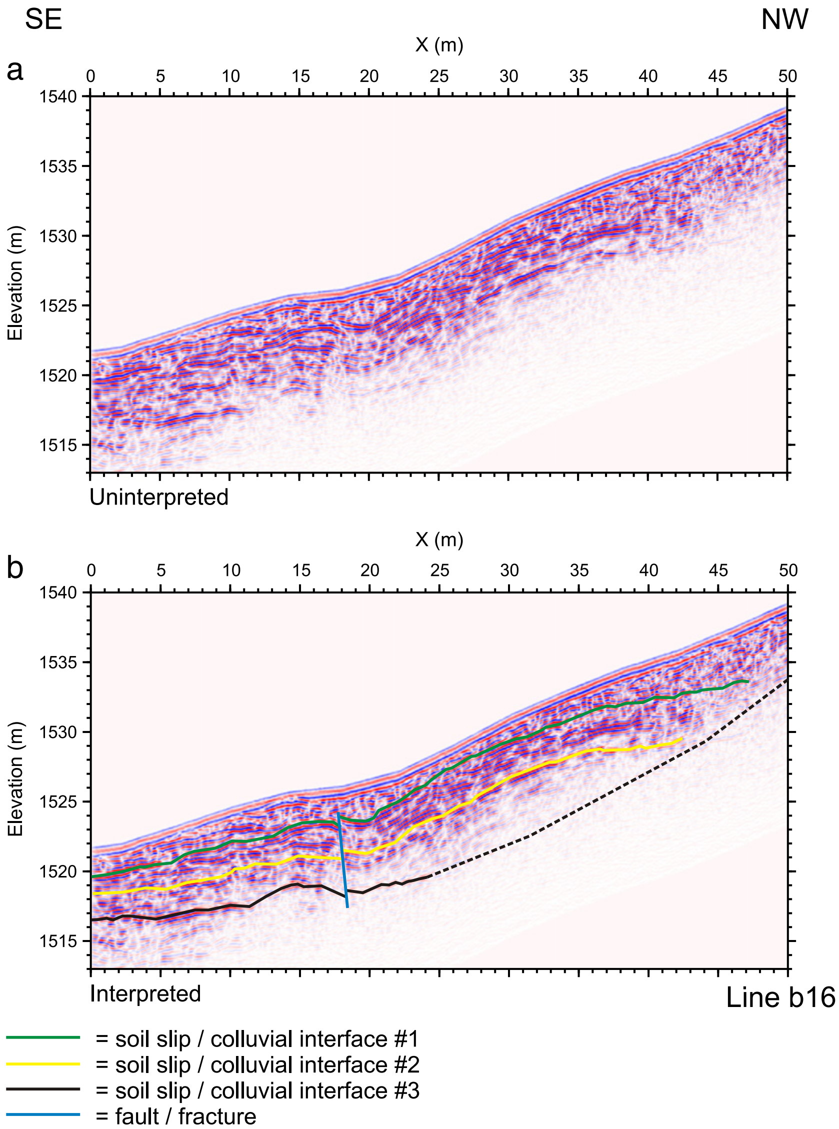

Fig. 8. a) Uninterpreted 250 MHz GPR profile b16. This profile is located at the base of the observed shallow landslides (Fig. 4). It displays a fundamentally different GPR reflectivity pattern than the profiles b3 and b5. The larger depth penetration suggests that the clay layer, a possible sliding plane for the shallow landslides, runs much deeper here. b) Interpreted profile b16. Strong and continuous curved reflections with clear interfaces suggest many older deposited shallow landslides (green, yellow, black), which underwent heavy folding afterwards by the load of the creeping soil upslope. The truncation in all reflections at $X = 17$ m is probably an overthrust (blue line) associated with the heavy folding. (For interpretation of the references to color in this figure legend, the reader is referred to the web version of this article.)

processes. Already we can state that the assumptions made in shallow landslide models such as the TOPKAPI algorithm are not representative (constant soil properties per gridcell and parallel-to-surface soil interfaces). Especially the assumption of 1D parallel-to-surface soil-interfaces and bedrock is disproved by our data. Since all three interfaces (schist layer, clay layer, bedrock) identified in our geophysical images are strong barriers for water, an extensive modeling study should explore the effects of subsurface topography on groundwater flow. Results from such a study can shed light on the dynamic timing of shallow landslides that is currently not well-reproduced by the shallow landslide algorithms like those implemented in the distributed TOPKAPI model.

7. Conclusions

For the improved understanding of shallow landslide composition, occurrence and susceptibility on steep alpine slopes, a combination of near surface geophysical methods has delineated the geometry and soil interfaces of past and present shallow landslides in the Urseren Valley. Trench, GPS, GPR and ERT data were collected on the slopes of the Urseren Valley near Hospental. The GPR and trenching data were particularly revealing as they imaged three major soil-interfaces that play an important role in shallow landslides. From the surface downwards, a xenolithic schist layer, clay layer and weathered bedrock were encountered, of which all three are major hydrological barriers. The clay layer is the most likely candidate for being a sliding plane during shallow landslides, even though the shallow schist layer facilitated the most recent large shallow landslide in October 2008.

Trench, GPR and ERT data showed that all three soil interfaces have significant topography associated with them, which can be caused by several processes. Interbedding of the schistose bedrock, causing differential weathering along the slope, can lead to different thicknesses and depths of the overlying soil layer. Alternatively, gravity pull and differential creep can move patches of soil down, causing differential compressional stress and thus folding of the soil layers. Extensive surface cracks in the soil layer support the idea of differential creep among the soil units. When steady creep turns into an actual shallow landslide under the influence of groundwater flow, the soil

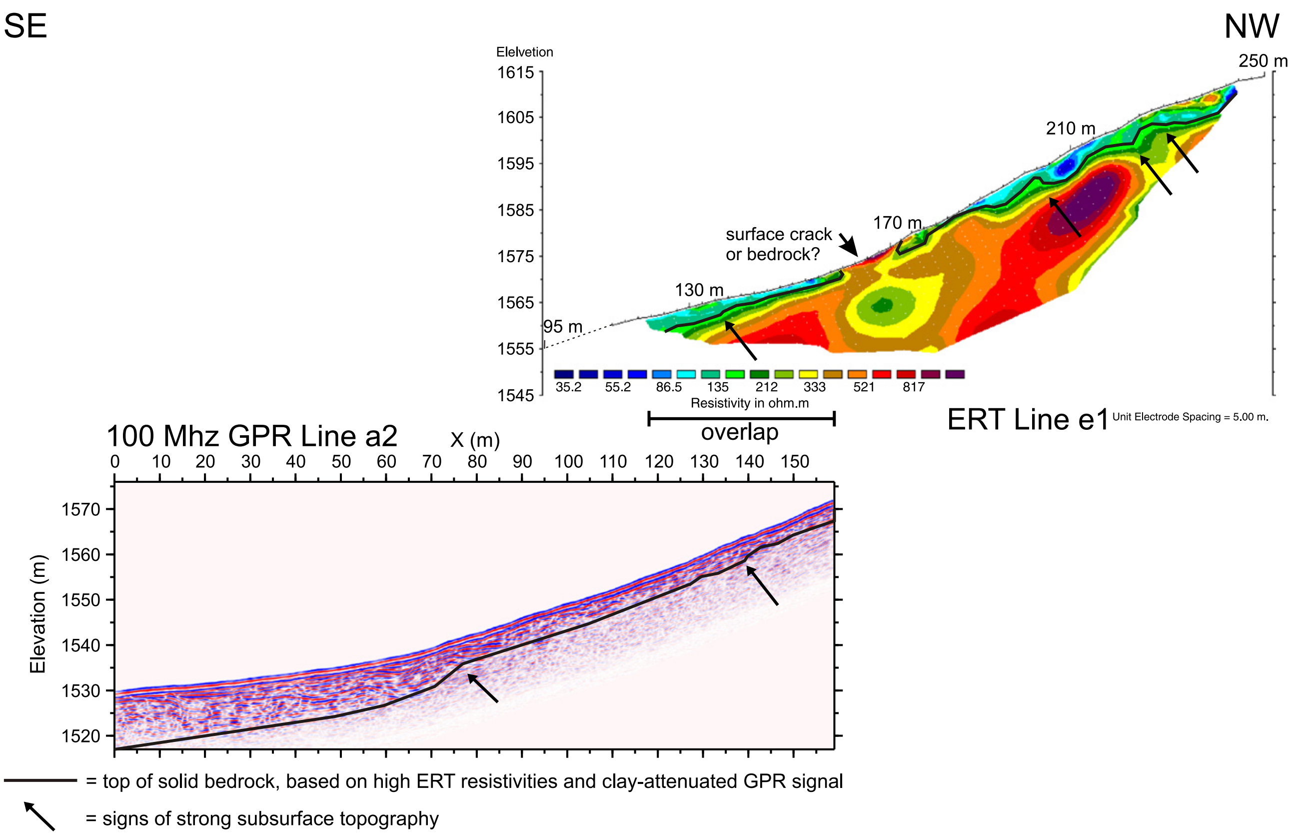

Fig. 9. Comparison between ERT profile e1 and proximate 100 MHz GPR profile a2. Both profiles sample part of the same slope, going from the upper steep part to the lower flat part (Fig. 4). Where they overlap, both types of data agree on the inferred depth of the solid bedrock (highly resistive feature, >250 Ω m, at ~5 m depth) and clay layer (bottom of conductive feature, <100 Ω m, at ~2 m depth). Both types of data also indicate short-wavelength undulations of the inferred clay layer over the whole length of the combined profiles, indicated by the thin black arrows.

layer is dumped at the base of the slopes if it has sufficient mechanical momentum. From GPR images at the base of the slopes we have interpreted the existence of a 'shallow landslide deposition zone', where many shallow landslides are stacked.

The good match between the soil-interfaces as identified in both trench data and GPR/ERT data reinforces the interpretation of the soil composition and validates its extrapolation. This demonstrates the added value of geophysical methods in delineating landslides and their hydrogeological organization. It must be said though that geophysical methods used in this study cannot cover an entire water catchment area, such that the measurements on small scale (±100 m) still have to be extrapolated to larger scale (10 km). A way to achieve this is to develop a statistical model of subsurface topography and incorporate this in the large scale water flow modeling. Another possibility is to employ high-resolution airborne geophysical methods like airborne GPR or hyperspectral EM methods.

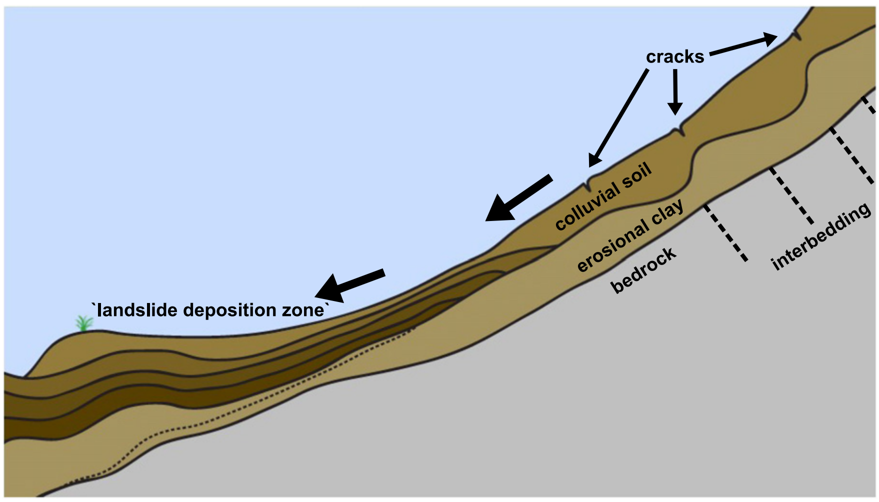

Fig. 10. Conceptual shallow landslide model resulting from combined interpretation of trench, GPS, GPR, and ERT data. In this conceptual model, 1) patches of soil steadily creep down, 2) leave opened and closed cracks in between, 3) get 'locked' by bedrock interbedding or subsurface topography, 4) episodically slip down and 5) get dumped in a 'shallow landslide deposition zone'.

Acknowledgements

The authors wish to thank David Finger, Katharina Edmaier and Nadine Konz for their enthusiastic and valuable help in the data acquisition. Further, the Swiss National Science Foundation and the APUNCH project are thanked for funding support. We used Landmark software for the GPR processing. We acknowledge support for this research by Landmark Graphics Corporation via the Landmark University Grant Program. Lastly, we appreciate the constructive comments of Dave Petley and an anonymous reviewer which have considerably improved our manuscript.

References

Anagnostopoulos, G.G., Burlando, P., 2011. Object-oriented computational framework for the simulation of variably saturated flow in soils, using a reduced complexity model. Submitted in Environmental Modelling and Software.

Annan, A.P., 2009. Electromagnetic principles of ground penetrating radar. In: Harry, M.J. (Ed.), Ground Penetrating Radar Theory and Applications. Elsevier, Amsterdam, pp. 1–40.

Blume, H.-P., 2002. Lehrbuch der Bodenkunde, 15th ed. Spektrum Akademischer Verlag GmbH, Heidelberg. 593 pp.

Büker, F., Green, A.G., Horstmeyer, H., 1998. Shallow seismic reflection study of a glaciated valley. Geophysics 63, 1395–1407.

Cadisch, J., Niggli, P., Rutsch, R., Gunzler-Seiffert, H., Huttenlocher, H., Burri, C., Wenk, E., Wells, M.K., 1948. An account of the long field meeting held in Switzerland: 6th–21st September, 1947. Proceedings of the Geologists' Association 59 (4), IN181–IN187.

Fahs, M., Younes, A., Lehmann, F., 2009. An easy and efficient combination of the mixed finite element method and the method of lines for the resolution of Richards' equation. Environmental Modelling and Software 24 (9), 1122–1126.

Fredlund, D.G., Xing, A., Fredlund, M.D., Barbour, S.L., 1995. The relationship of the unsaturated soil shear strength to the soil water characteristic curve. Canadian Geotechnical Journal 32, 440–448.

Gazdag, J., 1978. Wave equation migration with the phase-shift method. Geophysics 43, 1342–1351, http://dx.doi.org/10.1190/1.1440899.

Godt, J.W., Baum, R.L., Lu, N., 2009. Landsliding in partially saturated materials. Geophysical Research Letters 36 (2).

Green, A.G., Maurer, H.R., Spillmann, T., Heincke, B., Willenberg, H., 2006. High-resolution geophysical techniques for improving hazard assessments of unstable rock slopes. The Leading Edge 25, 311–316.

Heincke, B., Maurer, H.R., Green, A.G., Willenberg, H., Spillmann, T., Burlini, L., 2006. Characterizing an unstable mountain slope using shallow 2- and 3-D seismic tomography. Geophysics 71, B241–B256.

Konz, M., Chiari, M., Rimkus, S., Turowski, J.M., Molnar, P., Rickenmann, D., Burlando, P., 2011. Sediment transport modelling in a distributed physically based hydrological catchment model. Hydrology and Earth System Sciences 15, 2821–2837.

Lambe, T.W., Whitman, R.V., 1979. Soil Mechanics. John Wiley & Sons, New York.

Loke, M.H., Barker, R.D., 1996. Rapid least-squares inversion of apparent resistivity pseudosections by a quasi-Newton method. Geophysical Prospecting 44, 131–151.

Lu, N., Godt, J., 2008. Infinite slope stability under steady unsaturated seepage conditions. Water Resources Research 44 (11).

Meusburger, K., Alewell, C., 2008. Impacts of anthropogenic and environmental factors on the occurrence of soil slips in an alpine catchment (Urseren Valley, Switzerland). Natural Hazards and Earth System Sciences 8, 509–520.

Meusburger, K., Alewell, C., 2009. On the influence of temporal change on the validity of landslide susceptibility maps. Natural Hazards and Earth System Sciences 9, 1495–1507.

Pfiffner, A.O., 2009. Geologie der Alpen, 1st ed. Haupt Verlag, Bern. 357 pp.

Rahardjo, H., Lim, T., Chang, M., Fredlund, D., 1995. Shear-strength characteristics of a residual soil. Canadian Geotechnical Journal 32 (1), 60–77.

Schoeck, K., 2010. Simulation of soil slip occurrences with the distributed hydrological model TOPKAPI. MSc thesis, ETH Zurich, Switzerland.

Spillmann, T., Maurer, H.R., Willenberg, H., Evans, K.F., Heincke, B., Green, A.G., 2007. Characterization of an unstable rock mass based on borehole logs and diverse borehole radar data. Journal of Applied Geophysics 61, 16–38.

Telford, W.M., Geldart, L.P., Sheriff, R.E., 1990. Applied Geophysics, second edition. Cambridge University Press.

Terzaghi, K., 1943. Theoretical Soil Mechanics. John Wiley and Sons, New York.

Todini, E., Ciarapica, L., 2001. The TOPKAPI model. In: Singh, V.P., Frevert, D.K. (Eds.), Mathematical Models of Large Watershed Hydrology. Water Resources Publications, LLC, Littleton.

Todini, E., Mazzetti, C., 2008. TOPKAPI User's Manual and References. Progea Srl, Bologna.

Willenberg, H., Löw, S., Eberhardt, E., Evans, K.F., Spillmann, T., Heincke, B., Maurer, H.R., Green, A.G., 2008. Internal structure and deformation of an active slope instability in crystalline rock above Randa (Switzerland): Part I—Internal structure from integrated geological and geophysical investigation. Engineering Geology 101, 1–14.

Wyss, R., 1986. Die Urseren-Zone—Lithostatigraphie und Tektonik. Eclogae Geologicae Helvetiae 79, 731–767.